

Immune microenvironment-reshaping Au@Bi₂Te₃ nanoparticles for spectral computed tomography/photoacoustic imaging-guided synergetic photo/radio/immunotherapy

Kai Zhu^{1,2,§}, Zede Wu^{1,2,§}, Qiuyu Li², Meirong Hou^{1,2}, Honglei Hu^{1,2}, Shuting Zheng^{1,2}, Li Qi³, Yikai Xu¹ (✉), Chenggong Yan^{1,4} (✉), and Bingxia Zhao^{2,5} (✉)

¹ Department of Medical Imaging Center, Nanfang Hospital, Southern Medical University, Guangzhou 510515, China

² Guangzhou Key Laboratory of Tumor Immunology Research, Cancer Research Institute, School of Basic Medical Sciences, Southern Medical University, Guangzhou 510515, China

³ Guangdong Provincial Key Laboratory of Medical Image Processing, Guangdong Province Engineering Laboratory for Medical Imaging and Diagnostic Technology, School of Biomedical Engineering, Southern Medical University, Guangzhou 510515, China

⁴ Guangdong Provincial Key Laboratory of Shock and Microcirculation, Guangzhou 510515, China

⁵ Experimental Education/Administration Center, School of Basic Medical Science, Southern Medical University, Guangzhou 510515, China

§ Kai Zhu and Zede Wu contributed equally to this work.

© Tsinghua University Press 2022

Received: 15 March 2022 / Revised: 7 June 2022 / Accepted: 9 June 2022

ABSTRACT

Radiotherapy (RT) mediated tumor immunogenicity offers an opportunity for simultaneous RT and immunotherapy via immunogenic cell death (ICD), which releases damaged-associated molecular patterns and generates “eat me” signals for the innate immune system to modulate the immunogenicity. However, tumor hypoxia significantly reduces the therapeutic efficacy of RT and hampers its mediation of ICD induction. Herein, Au@Bi₂Te₃-polyethylene glycol (PEG) was rationally constructed as theranostic nanozymes for mild photothermal therapy, tumor hypoxia modulation, and RT adjuvant cancer immunotherapy. The tumor-specific production of oxygen could not only augment the effects of RT by enhanced reactive oxygen species (ROS) generation, but also reduce hypoxia-related cytokines and downregulate programmed cell death-ligand 1 (PD-L1) to unleash immune-enhancing T cells. Moreover, Au@Bi₂Te₃-PEG could act as an immune-blocking inhibitor by efficient ICD induction with the combination of mild-photothermal therapy + RT to inhibit the tumor immune escape and improve antitumor immune response. Increased amounts of CD4⁺ and CD8⁺ T cells and elevated levels of cytokines could be observed that eventually led to effective post-medication inhibition of primary and abscopal tumors. Spectral computed tomography/photoacoustic imaging allowed noninvasive and real-time tracking of nanoparticle (NP) accumulation and oxygenation status at tumor sites. Collectively, Au@Bi₂Te₃-PEG NPs could serve as effective theranostic nanoregulators with remarkable synergistic mild-photothermal/RT/immunotherapy effects that helped reshape the immune microenvironment and had remarkable molecular imaging properties.

KEYWORDS

radioresistance, immunotherapy, immunogenic cell death, hypoxia, programmed cell death-ligand 1 (PD-L1), spectral computed tomography (CT)

1 Introduction

Cancer immunotherapy, which is aimed at activating the immune system, has emerged as the third breakthrough in cancer treatment [1–3]. In recent years, with increasing recognition of the relationship between cancer and immunity, enormous strides have been made in cancer immunotherapy [4, 5]. For example, immune checkpoint blocking antibodies against programmed cell death protein 1/programmed cell death-ligand 1 (PD-1/PD-L1) have attracted tremendous attention [6, 7]. PD-1/PD-L1 blockade therapy has shown excellent therapeutic effects in various cancers [8, 9]. Although checkpoint blockade immunotherapy triggers prominent immune response in various cancers, the

response rate (10%–40%) is low, clinically [10, 11]. The main reasons for this include the low immunogenicity of tumor cells and inhibition of effector T cells in the immunosuppressive tumor microenvironment (TME) [12, 13].

Immunogenic cell death (ICD) involves release of damaged-associated molecular patterns (DAMPs) and generation of “eat me” signals to the innate immune system that promote immunogenicity [14–16]. DAMPs increase the maturation of dendritic cells (DCs) and enhance the antigen presentation to T lymphocytes to reverse the immunosuppressive TME [17, 18]. The combination of ICD inducers and PD-1/PD-L1 blockade therapy could be an effective strategy to enhance antitumor immune responses and suppress tumor growth [15, 19].

Address correspondence to Yikai Xu, yikaixu917@gmail.com; Chenggong Yan, ycgycg007@gmail.com; Bingxia Zhao, bingxiaz@foxmail.com, bingxiaz@gmail.com



Recently, many studies have demonstrated that radiotherapy (RT) can induce ICD through release of DAMPs and subsequent manipulation of the immunosuppressive TME [19, 20]. Although the exact mechanisms are still under investigation, distal tumor shrinking has been reported after RT of the primary tumor [19]. The abscopal effect indicates that immune response could be activated by RT. However, tumor recurrence and distant metastasis due to radioresistance are still critical issues that determine outcome and survival [20, 21].

Tremendous efforts have been made to design nanoparticles (NPs) with high-Z metal elements as radiosensitizers for inducing sensitization to radiotherapy [22–25]. However, one of the typical unfavorable characteristics of TME, hypoxia, remains a formidable challenge in RT and immunotherapy [12, 14, 26]. Reactive oxygen species (ROS)-mediated radiotherapeutic efficiency is highly related to oxygen concentration. Moreover, hypoxia can upregulate PD-L1 expression and decrease T lymphocyte infiltration [12]. Therefore, tumor-specific production of O_2 may not only increase the amount of ROS generation under irradiation, but also downregulate hypoxia-related cytokines (HIF-1 α) and PD-L1 to release T lymphocyte cells, which would be beneficial in improving radiotherapeutic efficiency and tumor immunotherapy [13, 27, 28].

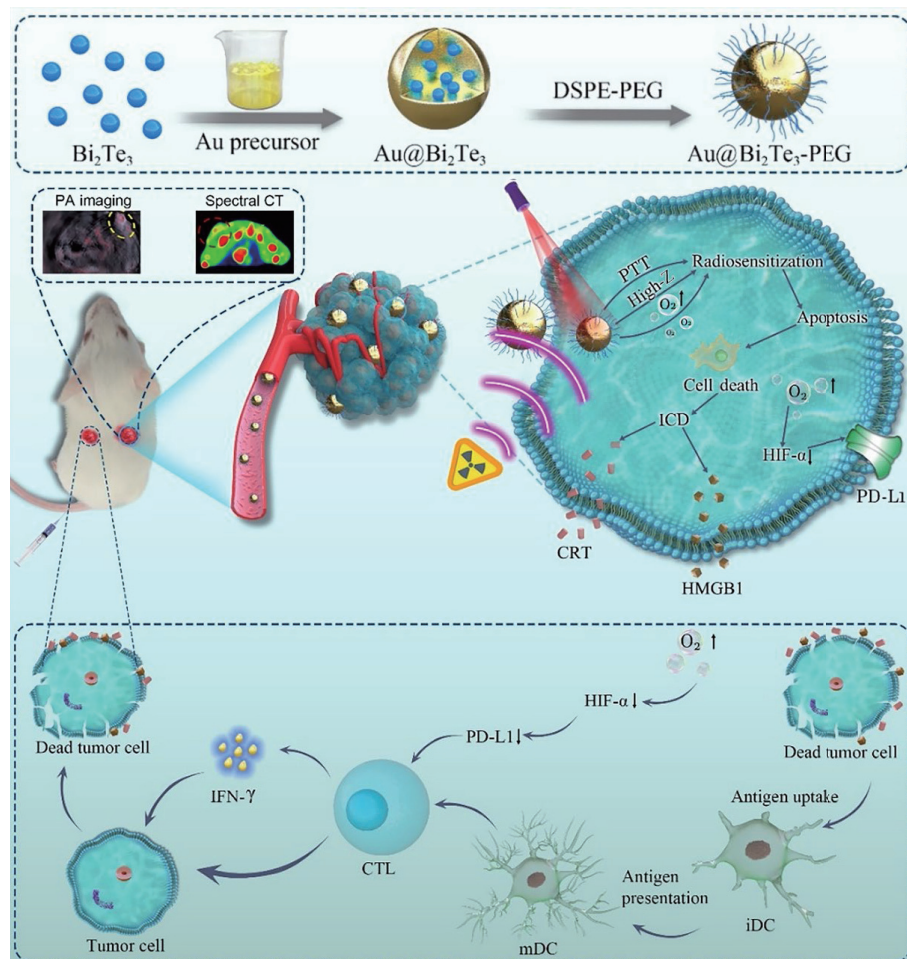
Recent studies have demonstrated that radiosensitizer Au-based NPs perform catalase (CAT) enzyme-like activity to generate O_2 *in situ* by catalyzing the overexpressed H_2O_2 ($100 \mu M^{-1}$) in the TME [29–31]. More recently, Long and co-workers revealed that enzyme-like activities of Au-containing NPs could be amplified by heavy metal such as Bi $^{3+}$, Pt $^{2+}$, Ag $^+$, and Hg $^{2+}$ [31–33].

Herein, aqueous ultra-small Bi $_2$ Te $_3$ nanodots with photothermal effect were first prepared by a simple and environmentally friendly method and then coated with Au shell (named as Au@Bi $_2$ Te $_3$) to stimulate CAT enzyme-like activity. The polyethylene glycol (PEG)-grafted Au@Bi $_2$ Te $_3$ nanoparticles (Au@Bi $_2$ Te $_3$ -PEG NPs) could be utilized for tumor-specific hypoxia relief, following the reduction of HIF-1 α and PD-L1, unleashing immune-promoting T cells. Moreover, hypoxia alleviation, photothermal conversion, and high-Z elements Au and Bi-mediated radiation energy deposition could synergistically enhance the efficacy of RT and induce ICD to inhibit tumor immune escape and evoke high immunogenicity of tumor cells. This integrated strategy facilitated DC maturation, CD8 $^+$ and CD4 $^+$ T cell recruitment, and cytokine release, which eventually led to the effective treatment of primary and distant tumors. Meanwhile, spectral computed tomography (CT) and photoacoustic (PA) imaging allowed noninvasive and real-time tracking of NPs accumulation in tumors. Above all, the designed Au@Bi $_2$ Te $_3$ -PEG NPs could be a promising nanoplateform for molecular imaging-guided synergistic mild-photothermal/RT/immunotherapy by reshaping the immune microenvironment (Scheme 1).

2 Materials and methods

2.1 Materials and reagents

Bismuth nitrate ($Bi(NO_3)_3 \cdot 5H_2O$, 99%), tellurium powder (Te), sodium borohydride ($NaBH_4$), DSPE-PEG ($M_W = 2,000$), and



Scheme 1 Schematic illustration of Au@Bi₂Te₃-PEG NPs as an H_2O_2 -driven oxygenator to alleviate tumor hypoxia and reshape immune microenvironment for spectral CT/photoacoustic imaging guided synergistic photo/radio/immunotherapy.

chloride trihydrate ($\text{HAuCl}_4 \cdot 3\text{H}_2\text{O}$, 99%) were purchased from Macklin (Beijing, China). CCK8 was obtained from Sigma-Aldrich (St. Louis, MO, USA). LIVE/DEAD Cell Imaging Kit and Dichlorofluorescein diacetate (DCFH-DA) were obtained from Solarbio (Guangzhou, China).

2.2 Preparation of Bi_2Te_3 and $\text{Au}@\text{Bi}_2\text{Te}_3$ -PEG

The synthesis of $\text{Au}@\text{Bi}_2\text{Te}_3$ nanostructure involved two stages. The first stage was the synthesis of Bi_2Te_3 and the second was the growth of Au onto the Bi_2Te_3 NPs. First, bismuth nitrate (243 mg) was mixed with 50 mL ethylene glycol in a flask. Second, 95.7 mg tellurium powder and 37 mg sodium borohydride were mixed with 5 mL deionized (DI) water in another flask. The solution was heated to 60 °C until the solution color turned to purple. The whole reaction was conducted under N_2 atmosphere. Third, the solution was quickly injected into bismuth nitrate solution and the reaction was continued for 10 min. The precipitates were washed with DI water followed by storage at 4 °C.

A total of 50 mg of Bi_2Te_3 NPs were dissolved in DI water, then 200 μL of 48.56 mM HAuCl_4 aqueous solution was added and stirred for 6 h. Finally, 120 μL of 100 mM NaBH_4 aqueous solution was added to reduce Au^{3+} to Au. $\text{Au}@\text{Bi}_2\text{Te}_3$ was obtained and washed three times with DI water.

To improve the biocompatibility, 20 mg of $\text{Au}@\text{Bi}_2\text{Te}_3$ NPs powder was dissolved in 20 mL pure water and ultrasonicated for 30 min. Then, DSPE-PEG (2,000 D) was added to $\text{Au}@\text{Bi}_2\text{Te}_3$ NPs solution, and stirred for 30 min under dark conditions. The resulting PEGylated NPs were centrifuged at 10,000g and washed with DI water three times followed by storage at 4 °C.

2.3 Characterization

The size and morphology assessment and elemental analysis of $\text{Au}@\text{Bi}_2\text{Te}_3$ were done by high resolution transmission electron microscopy (HRTEM) (JEOL 2100F, Japan). Zeta potential was performed by Zetasizer Nano ZS (Malvern, UK). Powder X-ray diffraction (PXRD) was chosen to test the crystal structures of $\text{Au}@\text{Bi}_2\text{Te}_3$ NPs. X-ray irradiation was performed using a cabinet X-Ray Irradiation System (Faxitron MultiRad225, USA).

2.4 Evaluation of the oxygen production capacity of $\text{Au}@\text{Bi}_2\text{Te}_3$ -PEG

To test the oxygen production capacity of the $\text{Au}@\text{Bi}_2\text{Te}_3$ -PEG NPs, $\text{Au}@\text{Bi}_2\text{Te}_3$ -PEG was dispersed in 5 mL of PBS (pH = 6.5 or 7.4) containing H_2O_2 (1 mmol/L), and the concentration of $\text{Au}@\text{Bi}_2\text{Te}_3$ -PEG was found to be 100 $\mu\text{g/mL}$. The dissolved oxygen meter was used to determine the oxygen concentration in the above solution (DO200, Clean, China).

2.5 Evaluation of photothermal performance of $\text{Au}@\text{Bi}_2\text{Te}_3$ -PEG

$\text{Au}@\text{Bi}_2\text{Te}_3$ -PEG NP solutions (1 mL) of different concentrations (0, 50, 75, 100, 150, and 200 ppm) were irradiated for 5 min at different power densities (0.3, 0.5, 0.7, and 1 W/cm²). The temperature changes of $\text{Au}@\text{Bi}_2\text{Te}_3$ -PEG NP solutions were recorded by thermal imaging system. Finally, photothermal stability of $\text{Au}@\text{Bi}_2\text{Te}_3$ -PEG (200 ppm) was tested for five cycles at 0.7 W/cm².

2.6 In vitro spectral CT and PA imaging

The contrast enhancement performance of $\text{Au}@\text{Bi}_2\text{Te}_3$ -PEG was compared with commercial iopromide using spectral CT (GE revolution CT, Healthcare). The imaging parameters were: tube voltage of 80/140 kV and tube current of 600 mA. The

concentrations were changed as follows: 0, 0.3125, 0.625, 1.25, 2.5, and 5 mg/mL.

To verify the performance of PA imaging capability of $\text{Au}@\text{Bi}_2\text{Te}_3$ -PEG, 200 μL of aqueously dispersed $\text{Au}@\text{Bi}_2\text{Te}_3$ -PEG NPs (0, 50, 75, 100, 150, and 200 $\mu\text{g/mL}$) was scanned by the MOST Invision PA System. The imaging parameters were as follows: frequency of 50 MHz, PA gain of 60 dB, and 2D gain of 22 dB. The PA signal and HbO_2 were analyzed by the View MOST™ software.

2.7 Cellular ROS detection *in vitro*

The 4T1 cell lines were donated by the Clinical Medicine Center at Nanfang Hospital (Guangzhou, China). Four groups studied were: PBS, $\text{Au}@\text{Bi}_2\text{Te}_3$ -PEG, RT, and $\text{Au}@\text{Bi}_2\text{Te}_3$ -PEG + RT groups. The RT and $\text{Au}@\text{Bi}_2\text{Te}_3$ -PEG + RT groups received 4 Gy of irradiation. After 24 h incubation, DCFH-DA (10 μM) was added and further incubation for 30 min was done. Finally, the cells were photographed by fluorescence microscopy (Olympus IX71, Japan).

2.8 Cytotoxicity assay

The 4T1 cells were seeded in 96-well plates with density of 6,000 cells/well and cultivated to attach for 24 h. Then, 100 μL $\text{Au}@\text{Bi}_2\text{Te}_3$ -PEG NPs of different concentrations (0, 12.5, 25, 50, 100, and 150 ppm) were added to each well. Another 24 h incubation was followed by staining with CCK8 (5 mg/mL) for 1 h. Finally, the cells were analyzed by an enzyme-linked reader (BIOTEK ELX80, the Netherlands).

2.9 In vitro anti-tumor studies

The cell viabilities were evaluated in the following groups with different treatments: PBS, $\text{Au}@\text{Bi}_2\text{Te}_3$ -PEG, $\text{Au}@\text{Bi}_2\text{Te}_3$ -PEG + NIR, $\text{Au}@\text{Bi}_2\text{Te}_3$ -PEG + RT, and $\text{Au}@\text{Bi}_2\text{Te}_3$ -PEG + NIR + RT. Then, different interventions were carried out with the procedure being the same as the cytotoxicity study *in vitro*. The incubating time was 24 h after PTT and RT. Then, cells were stained for live/dead for 1 h, and photographed by fluorescence microscopy.

2.10 Clonogenic assay

The 4T1 cells were inoculated in 6-well plates (1,000 cells/well). After 24 h, preculture, 2 mL of culture medium with or without $\text{Au}@\text{Bi}_2\text{Te}_3$ -PEG (100 $\mu\text{g/mL}$) was added. After 24 h incubation, varying irradiation (0, 2, 4, and 6 Gy) was imposed on cells. X-ray irradiation was performed using a cabinet X-Ray Irradiation System (Faxitron MultiRad225, USA). Voltage: 225 kV, Dose rate: 1.5 Gy/min. Subsequently, the treated cells were cultured for 7 days. Afterwards, the cells were fixed with methanol and stained with Crystal Violet, and then captured by a digital camera.

2.11 Detection of ICD and DC biomarkers *in vitro*

The 4T1 cells were seeded in a confocal dish (10,000 cells/well) and were divided into six groups: (1) PBS, (2) $\text{Au}@\text{Bi}_2\text{Te}_3$ -PEG, (3) RT, (4) $\text{Au}@\text{Bi}_2\text{Te}_3$ -PEG + NIR, (5) $\text{Au}@\text{Bi}_2\text{Te}_3$ -PEG + RT, and (6) $\text{Au}@\text{Bi}_2\text{Te}_3$ -PEG + NIR + RT. Then 200 μL PBS or 200 $\mu\text{g/mL}$ $\text{Au}@\text{Bi}_2\text{Te}_3$ -PEG solution was added to the confocal dish. 6 Gy irradiation (voltage: 225 kV, dose rate: 1.5 Gy/min) to cells was performed. After 24 h of incubation, cells were fixed and permeabilized. Cells were further incubated with CRT, HMGB1 antibodies to 4 °C overnight. PE or fluorescein (FITC) labelled with secondary antibodies against rabbits in goats were then incubated with fixed 4T1 under dark conditions for 1 h. Finally, expression levels of CRT and HMGB1 were captured by fluorescence microscopy.

The 4T1 cells were seeded in a confocal dish (10,000 cells/well)

and were divided into six groups: (1) PBS, (2) Au@Bi₂Te₃-PEG, (3) RT, (4) Au@Bi₂Te₃-PEG + NIR, (5) Au@Bi₂Te₃-PEG + RT, and (6) Au@Bi₂Te₃-PEG + NIR + RT. Then 200 μL PBS or 200 μg/mL Au@Bi₂Te₃-PEG solution was added to the dish. 6 Gy irradiation (voltage: 225 kV, dose rate: 1.5 Gy/min) to cells was performed. After being irradiated with RT and NIR, the 4T1 cells were incubated with BMDCs. After 24 h, the BMDCs were stained with APC anti-CD86, PE-CD80 and PE-Cy7 anti-CD11c and DCs maturation was then analyzed by flow cytometry analysis.

2.12 Animal experiments

Nanfang Hospital animal center of Southern Medical University (Guangzhou, China) provided the female BALB/c mice (5–6 weeks). All experimental steps complied with regulations of the Animal Ethics Committee in China. The 4T1 tumor-bearing mice were exografted through subcutaneous inoculation of 1 × 10⁶ cells onto the right back of the mice. The experiments were performed when the tumor volume reached 50–60 mm³.

2.13 In vivo spectral CT/PA imaging

Prior to imaging experiments, 4T1 tumor-bearing mice were anesthetized with sodium pentobarbital. After that, 100 μL Au@Bi₂Te₃-PEG NPs (200 μg/mL) (experiment, $n = 3$) was intravenously injected through the tail vein. PA images were obtained at 0, 1, 3, 6, 8, 10, 12, and 24 h post-injection. The wavelength ranged from 680–900 nm. At PA signal of 808 nm, oxygenated hemoglobin (HbO₂) and deoxyhemoglobin (Hb) were analyzed by the View MOST™ software. For *in vivo* spectral CT imaging, 200 μL Au@Bi₂Te₃-PEG NPs (10 mg/mL) was intravenously administered and scanned by using spectral CT ($n = 3$). The spectral CT imaging parameters were the same as mentioned above.

2.14 In vivo anti-primary tumor studies

The 4T1 tumor-bearing mice were randomly divided into seven groups ($n = 5$): (1) PBS, (2) NIR, (3) RT, (4) Au@Bi₂Te₃-PEG, (5) Au@Bi₂Te₃-PEG + NIR, (6) Au@Bi₂Te₃-PEG + RT, and (7) Au@Bi₂Te₃-PEG + NIR + RT. Then, 200 μL PBS or 200 μg/mL Au@Bi₂Te₃-PEG solution was intravenously injected through the tail vein. The NIR power density was 0.7 W/cm² for 5 min. Radiation dose was set as 6 Gy (voltage: 225 kV, dose rate: 1.5 Gy/min). The body weights were also taken every 2 days during the treatment period. After 21 days, the tumors tissues and main organs of mice were stained with hematoxylin and eosin (H&E) and Ki67 staining.

2.15 In vivo distant tumor inhibition

To establish distant tumor model, 1 × 10⁶ 4T1 cells were subcutaneously injected onto right back of the mice (primary tumor); when the tumor volumes grew to 40–50 mm³, the mice were randomly divided into six groups ($n = 4$): (1) PBS, (2) Au@Bi₂Te₃-PEG, (3) RT, (4) Au@Bi₂Te₃-PEG + NIR, (5) Au@Bi₂Te₃-PEG + RT, and (6) Au@Bi₂Te₃-PEG + NIR + RT. A total of 200 ppm Au@Bi₂Te₃-PEG solution or 200 μL PBS was intravenously administered into the mice. The RT treatment was performed as mentioned above. After 24 h of treatment, 1.25 × 10⁵ cells were implanted into the left back (distant tumor).

To quantitatively evaluate PD-L1 expression and CD4/CD8 T cells, distant tumors were harvested at 14 days after treatment. The tumor tissues were digested with papain enzyme to make a single cell suspension. The collected cells were then incubated with APC-Cy7 anti-CD45, APC anti-CD3, FITC anti-CD4, and PreCP-Cy5.5 anti-CD8 to evaluate the content of CD4⁺ or CD8⁺ T cells in the tumors using flow cytometry, following standard protocols.

Finally, the frequency of mature DCs in the lymph nodes was examined by flow cytometry after immune fluorescence staining with APC anti-CD86, PE-Cy7 anti-CD11c, and PE anti-CD80. Moreover, cells were mixed with HIF-α antibody, PD-LI antibody (Abcam, Shanghai, China), and CD45, CD3, CD4, and CD8a antibodies (Cell Signaling Technology, Shanghai, China) for immunofluorescence and western blot analysis. Furthermore, IFN-γ, TNF-α, and IL-6 in mice serum were measurement by using ELISA kits.

2.16 Statistical analysis

Statistical analysis was performed using SPSS software (version 20.0, SPSS). Experimental data were expressed as mean ± standard deviation (SD). Paired *t*-test and one-way ANOVA analysis were used to analyze experimental data. *P* value < 0.05 was considered statistically significant.

3 Results and discussion

3.1 Synthesis and characterization of Au@Bi₂Te₃-PEG

Aqueous Bi₂Te₃ NPs were first synthesized via a facile one-pot approach (shown in Fig. S1 in the Electronic Supplementary Material (ESM)). Au shell was then deposited on Bi₂Te₃ NPs by reducing HAuCl₄ with NaBH₄ *in situ*. HRTEM images showed that the Au@Bi₂Te₃ NPs had spherical morphology and good dispersibility. The average diameter was 9.2 ± 1.8 nm (Figs. S1 and S2 in the ESM). To improve the water solubility and biocompatibility, Au@Bi₂Te₃ NPs were modified with DSPE-PEG. The surface zeta potential subsequently decreased from +6.8 mV for Au@Bi₂Te₃ to -11.7 mV for Au@Bi₂Te₃-PEG NPs (Fig. S3 in the ESM), indicating a successful modification with the negative charge, while the PEGylation had no influence on the morphology of the NPs (Fig. 1(a)). TEM-energy dispersive X-ray spectroscopy (EDS)-mapping and line-scanning results showed Au@Bi₂Te₃ NPs contained the elements Au, Bi, and Te and Bi₂Te₃ nanodots were inlayed in the Au nano structure (Fig. 1(b) and Fig. S4 in the ESM). The X-ray powder diffraction patterns indicated that peaks of Au@Bi₂Te₃ NPs matched with Au and Bi₂Te₃ (Fig. 1(c)). Taken together, the above results showed successful fabrication of Au@Bi₂Te₃-PEG NPs. The resultant Au@Bi₂Te₃-PEG NPs exhibited satisfactory stability in various physiological solutions (Fig. S5 in the ESM), thereby ensuring their further applications.

As Au-based nanoparticles have been reported to have catalase enzyme-like activity and generate O₂ *in situ* by catalyzing the overexpressed H₂O₂ (100 μM⁻¹) in TME, the oxygen production capacity of Au@Bi₂Te₃-PEG NPs was measured in a H₂O₂ solution [33]. The Au@Bi₂Te₃-PEG NPs exhibited obvious catalase enzyme-like activity and triggered efficient O₂ generation with H₂O₂, while no obvious oxygen generation could be observed by using Au, Au + free Bi₂Te₃, or Bi₂Te₃ NPs at the same concentration (Fig. 1(d) and Fig. S6(a) in the ESM); this demonstrated the integration of ultra-small Bi₂Te₃ nanodots with nano Au could be an efficient strategy to generate O₂. Moreover, the influence of pH on CAT enzyme-like activity of Au@Bi₂Te₃-PEG NPs was also studied. As shown in Fig. 1(e), and Figs. S6(b) in the ESM, Au@Bi₂Te₃-PEG NPs showed better catalytic activity at pH 6.5 than that at pH 7.4, which made them especially suitable for therapeutically targeting the acidic TME. This interesting phenomenon may be not consistent with previous studies which reported that under alkaline conditions Au NPs exhibited intrinsic CAT-like catalytic activity in that Au NPs could convert H₂O₂ into O₂ [33, 34]. As reported, the catalytic activities of Au NPs not only rely on pH value, but also are strongly dependent on the Au NP size, surface state, and so on. More importantly, the enzyme-like

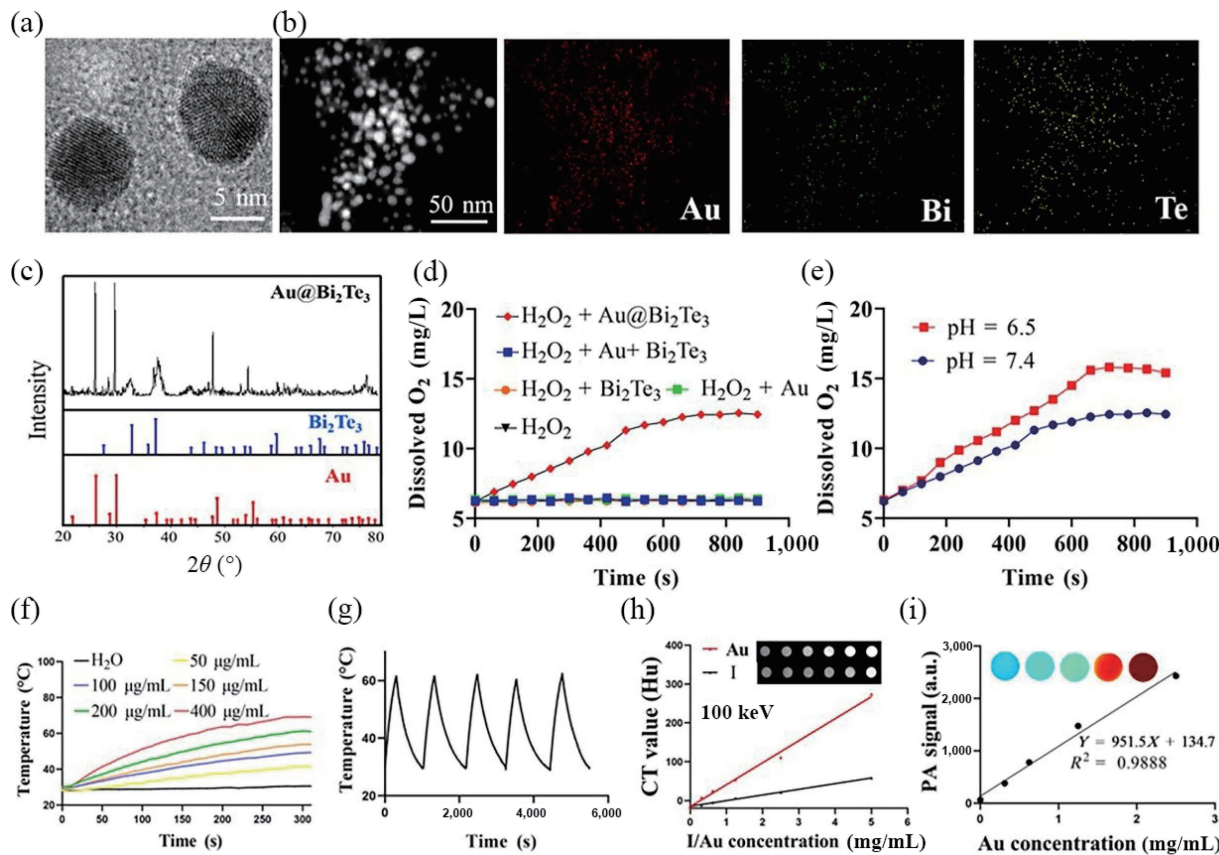


Figure 1 Synthesis and physicochemical characterization of $\text{Au}@\text{Bi}_2\text{Te}_3$ NPs. (a) High-resolution TEM images of $\text{Au}@\text{Bi}_2\text{Te}_3$. (b) Distribution of Au (red), Bi (green), and Te (yellow) elements through an $\text{Au}@\text{Bi}_2\text{Te}_3$ NPs by element mapping. (c) X-ray powder diffraction spectrum of $\text{Au}@\text{Bi}_2\text{Te}_3$ and corresponding fingerprints of crystalline indexes for Bi_2Te_3 and Au. (d) Quantitative oxygen generation by $\text{H}_2\text{O}_2 + \text{Au}@\text{Bi}_2\text{Te}_3$, $\text{H}_2\text{O}_2 + \text{Au} + \text{Bi}_2\text{Te}_3$, $\text{H}_2\text{O}_2 + \text{Bi}_2\text{Te}_3$, and H_2O_2 after reaction with H_2O_2 . (e) Quantitative oxygen generation with different pH of 6.5 and 7.4. (f) Temperature curves of $\text{Au}@\text{Bi}_2\text{Te}_3$ solution under the irradiation of 808 nm laser (0.7 W/cm^2 , 5 min) at different concentrations. (g) PTT stability of $\text{Au}@\text{Bi}_2\text{Te}_3$ NPs under NIR irradiation (0.7 W/cm^2). (h) Linear correlation between the CT intensity values of $\text{Au}@\text{Bi}_2\text{Te}_3$ NPs and iodine at different concentrations under 100 keV condition. (i) Linear correlation between average photoacoustic signal intensity and $\text{Au}@\text{Bi}_2\text{Te}_3$ NPs aqueous dispersion at different concentrations *in vitro*.

activities can be enhanced with the existence of several heavy metals, such as Bi^{3+} , Pt^{2+} , Ag^+ , or Hg^{2+} ions [32]. In the study by Lien et al., the Bi-Au NPs exhibited a significant activation of Au NP nanozymes. This amazing phenomenon is perhaps mainly due to the formation of a certain fraction of bimetallic Bi-Au complex. There is now no doubt that with the Bi_2Te_3 ultra-small core inside the Au shell, the catalytic activity of $\text{Au}@\text{Bi}_2\text{Te}_3$ -PEG NPs could be dramatically stimulated [33].

It is well established that Au- and Bi-based nanomaterials have desirable photothermal abilities; hence, $\text{Au}@\text{Bi}_2\text{Te}_3$ -PEG NPs were also presumed to possess photo-thermal conversion capability [34, 35]. To examine this hypothesis, the photothermal effect of $\text{Au}@\text{Bi}_2\text{Te}_3$ -PEG NPs was tested with 808 nm laser irradiation. The temperature of the $\text{Au}@\text{Bi}_2\text{Te}_3$ -PEG solution (200 $\mu\text{g/mL}$) rapidly rose to 62 $^\circ\text{C}$ within 5 min at 0.7 W/cm^2 , which is much higher than DI water (Fig. 1(f)). The temperature of $\text{Au}@\text{Bi}_2\text{Te}_3$ -PEG solutions increased rapidly over time in a laser power density-dependent manner (Fig. S7 in the ESM). Five successive cycles indicated stable photothermal property as seen in Fig. 1(g). These results indicated that $\text{Au}@\text{Bi}_2\text{Te}_3$ -PEG NPs could serve as photothermal agents that convert light to heat energy and could be employed in cancer photothermal therapy.

Furthermore, the capacity of $\text{Au}@\text{Bi}_2\text{Te}_3$ -PEG NPs as CT/PA imaging contrast agent was also assessed. The phantoms with increasing $\text{Au}@\text{Bi}_2\text{Te}_3$ -PEG NP concentrations exhibited desirable CT imaging contrast enhancement properties and concentration-dependent brightness (superior to clinically used iodine at all detected energies) (Fig. 1(h), and Figs. S8 and S9 in the ESM). PA imaging contrast enhancement could also be observed as

concentration-dependent brightness (Fig. 1(i)). The above results demonstrated the excellent imaging performance of $\text{Au}@\text{Bi}_2\text{Te}_3$ -PEG NPs on spectral CT and PA imaging.

3.2 *In vitro* cellular experiments

Encouraged by the potent superior property of $\text{Au}@\text{Bi}_2\text{Te}_3$ -PEG NPs, the cytotoxicity of $\text{Au}@\text{Bi}_2\text{Te}_3$ -PEG NPs was evaluated using the CCK-8 test. As indicated in Fig. 2(a), cell viabilities were maintained at more than 80% even at the highest concentration (150 $\mu\text{g/mL}$), which indicated the favorable biocompatibility of the synthesized $\text{Au}@\text{Bi}_2\text{Te}_3$ -PEG.

Due to the excellent oxygen production capacity of $\text{Au}@\text{Bi}_2\text{Te}_3$ -PEG NPs *in vitro*, tumor-specific production of O_2 was achieved, which further increased the amount of ROS generation under irradiation. The intracellular ROS production was then explored by DCFH-DA. As shown in Fig. 2(b), obviously increased ROS amount was seen in the $\text{Au}@\text{Bi}_2\text{Te}_3$ -PEG + RT group compared with the RT alone group, which could be explained by the fact that $\text{Au}@\text{Bi}_2\text{Te}_3$ -PEG promoted intracellular oxygenation for hypoxia alleviation, which facilitated ROS release.

Encouraged by the enhanced ROS generation, clonogenic assay was performed to determine the efficiency of $\text{Au}@\text{Bi}_2\text{Te}_3$ -PEG NPs as a radiosensitizer. As shown in Fig. 2(c), the $\text{Au}@\text{Bi}_2\text{Te}_3$ -PEG + RT group showed lower cell viabilities than the RT alone group, thus verifying the RT sensitization effect of the $\text{Au}@\text{Bi}_2\text{Te}_3$ -PEG NPs. As the radiation dose increased (0, 2, 4, and 6 Gy), the survival fractions of 4T1 cells decreased significantly. These results indicated $\text{Au}@\text{Bi}_2\text{Te}_3$ -PEG was a prominent radiosensitizer that inhibited tumor growths that were irradiated.

Moreover, as the $\text{Au}@\text{Bi}_2\text{Te}_3$ -PEG NPs possessed excellent

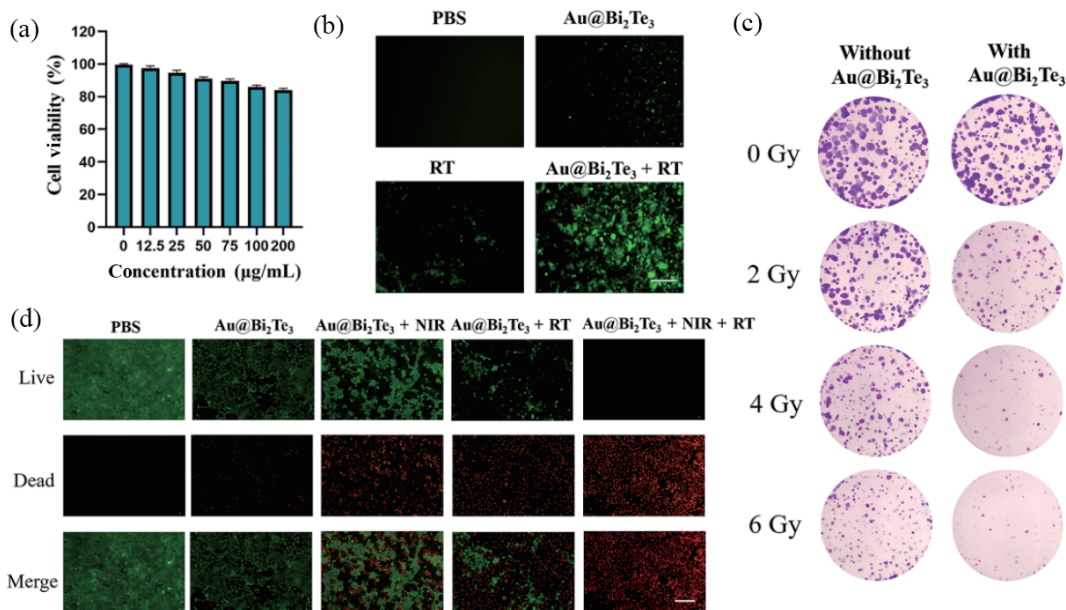


Figure 2 (a) Relative viabilities of 4T1 cells incubated with different Au@Bi₂Te₃-PEG concentrations. (b) Fluorescent images stained by DCFH-DA to explore intracellular ROS production. (c) Colony formation of 4T1 cells with different treatments. (d) Live/dead fluorescent images of 4T1 cells stained by Calcein-AM/PI. Bar indicates 100 μm .

photothermal conversion capability, a mild photothermal therapy ($\sim 45^\circ\text{C}$, mPTT) was then applied as it has been reported that better therapeutic effect could be obtained by the combination of RT with mPTT. The CCK-8 and Live/Dead assay were designed to validate the synergistic effect of RT and mPTT. As shown in Fig. S10 in the ESM and Fig. 2(d), the most prominent cellular cytotoxicity was found in the Au@Bi₂Te₃-PEG + NIR + RT group, which confirmed the synergistic RT/mPTT effect on 4T1 cells.

3.3 Tumor accumulation of NPs and hypoxia alleviation

To verify the optimized time point for the enhanced RT *in vivo*, the accumulation of Au@Bi₂Te₃-PEG NPs at the tumor site was assessed by spectral CT and PA imaging. *In vivo* molecular imaging indicated the signal intensity of Au@Bi₂Te₃ NPs in the tumor site brightened gradually and reached a peak at 8–9 h after intravenous injection (Figs. 3(a)–3(d)).

Moreover, tumor hypoxia level was evaluated by PA imaging based on the 680 nm optical absorption of oxygenated hemoglobin (HbO₂), which is indicative of the O₂ concentration in tumor vessels [30, 36, 37]. Compared to the baseline (5.5% \pm 0.7%), the HbO₂ of the tumor was significantly increased (20.8% \pm 2.5%) at 10 h post-injection, and reached a peak at 10 h post-injection. The tumor hypoxic status was also monitored by the PA images of the Hb, which showed a reverse trend to that of HbO₂ with a trough at 10 h post-injection (Figs. 3(e)–3(g) and Fig. S12 in the ESM). The hypoxia relief was further confirmed by detecting HIF-1 α levels, which is presently the pivotal indicator of tumor hypoxic status [13, 27]. Compared to the PBS group, the tumor tissues from the Au@Bi₂Te₃-PEG group showed significant decrease in hypoxia area, as evidenced by the immunofluorescence staining and western blot analysis of HIF-1 α protein in 4T1 tumors (Figs. 3(h)–3(j)). These results demonstrated that the Au@Bi₂Te₃-PEG NPs were transported to tumor hypoxic region, and then reacted with H₂O₂ in tumoral acidic microenvironment to efficiently release O₂.

3.4 In vivo primary tumor therapy

In view of the synergistic mild-PTT/RT effect of Au@Bi₂Te₃-PEG *in vitro* and favorable tumor accumulation *in vivo*, the tumor inhibition potential of Au@Bi₂Te₃-PEG in tumor-bearing mice

was explored. The relative tumor volumes (V/V_0) post-treatment during 21 days are shown in Fig. 4(a) and Fig. S13 in the ESM. As expected, the Au@Bi₂Te₃-PEG + RT group had a more pronounced inhibitory effect than the RT group alone. This was mainly due to the efficient hypoxia alleviation and high-Z element-mediated RT sensitization of Au@Bi₂Te₃-PEG NPs. More importantly, the most obvious inhibitory effect was observed in the Au@Bi₂Te₃-PEG + NIR + RT group. The tumors almost completely melted without recurrence, which can be attributed to the synergistic effects of radiation energy depositions, mild hyperthermia, and tumor hypoxia rescue (Fig. 4(b)). Final body weights of each group 20 days post-treatment are depicted in Fig. 4(c). No significant weight loss was found in the groups, which proved that all treatments had negligible side effects. H&E and Ki67 staining also indicated that the Au@Bi₂Te₃-PEG + NIR + RT group exhibited the most obvious tumor damage (Figs. 4(d) and 4(e)).

3.5 ICD induction, cytokine secretion, and PD-L1 downregulation

As reported previously, ICD is induced by RT [19]. But the efficiency of mono-RT was not enough to activate effective anti-tumor immune response. Because enhanced RT could be mediated by the Au@Bi₂Te₃-PEG NPs, CRT exposure and the release of HMGB1 and ATP (three of the hallmarks when cells are undergoing ICD) were investigated to figure out whether ICD could be induced. ICD-related indicators were validated *in vitro* first, as shown in Fig. 5(a), and Figs. S14 and S15 in the ESM, the Au@Bi₂Te₃-PEG + RT group and the Au@Bi₂Te₃-PEG + NIR + RT group showed a greater CRT, HMGB1, and ATP expression, indicating an evident increase in RT-induced ICD. In contrast, all other groups showed low CRT and HMGB1 expression. CRT exposure was further evaluated *in vivo* to demonstrate ICD induction, as shown in Fig. S16(a) in the ESM, the Au@Bi₂Te₃-PEG + RT group and the Au@Bi₂Te₃-PEG + NIR + RT group also showed a greater CRT expression, which were consistent with the CRT *in vitro*.

To test whether the CRT exposure and HMGB1 release could activate DCs, CD80 and CD86 in DCs after different treatments were verified by flow cytometry *in vitro* and *in vivo* (Figs. 5(b) and

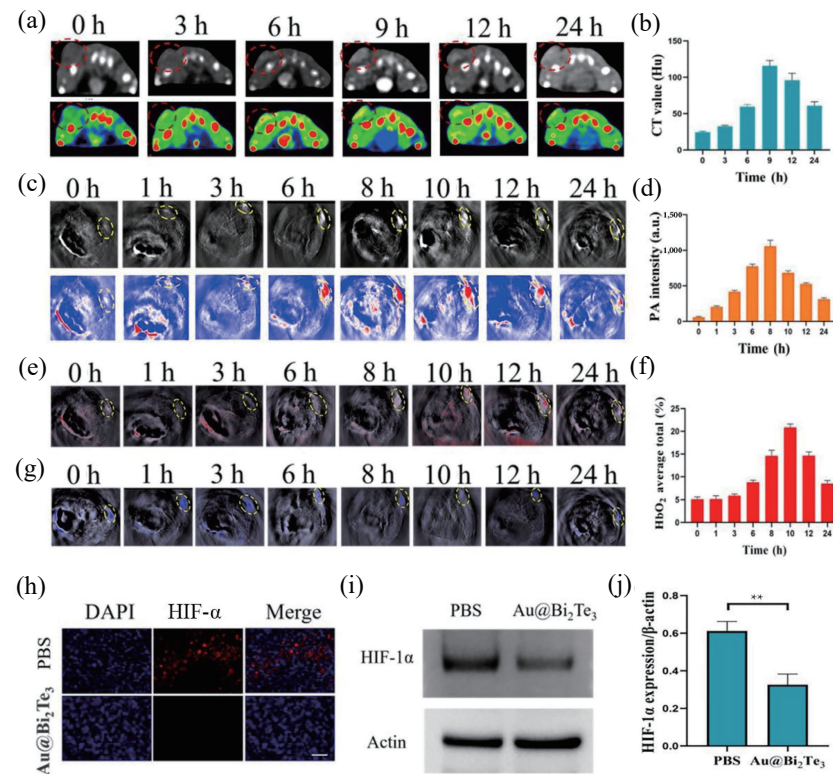


Figure 3 Spectral CT and PA imaging analysis of Au@Bi₂Te₃ NPs *in vivo*. (a) *In vivo* spectral CT and corresponding pseudo-color images of tumor-bearing mice before and after intravenous injection of the equivalent concentration of Au@Bi₂Te₃ NPs. (b) The CT intensity values in tumor sites after intravenous Au@Bi₂Te₃ NPs at different time points ($n = 3$). (c) *In vivo* PA imaging and corresponding pseudo-color images of 4T1 tumor-bearing mice before and after intravenous injection of Au@Bi₂Te₃ NPs. (d) The PA intensity values in tumor sites after intravenous Au@Bi₂Te₃ NPs at different time points ($n = 3$). (e) *In vivo* PA images of the (e) and (f) HbO₂ and (g) Hb after intravenous Au@Bi₂Te₃-PEG NPs ($n = 3$). (h) Immunofluorescence analysis of tumor HIF- α expression in the Au@Bi₂Te₃ NPs or PBS group. Bar indicates 100 μ m. (i) and (j) Western blot analysis of HIF- α protein in 4T1 tumors collected from tumor-bearing mice ($n = 3$). ** $P < 0.01$.

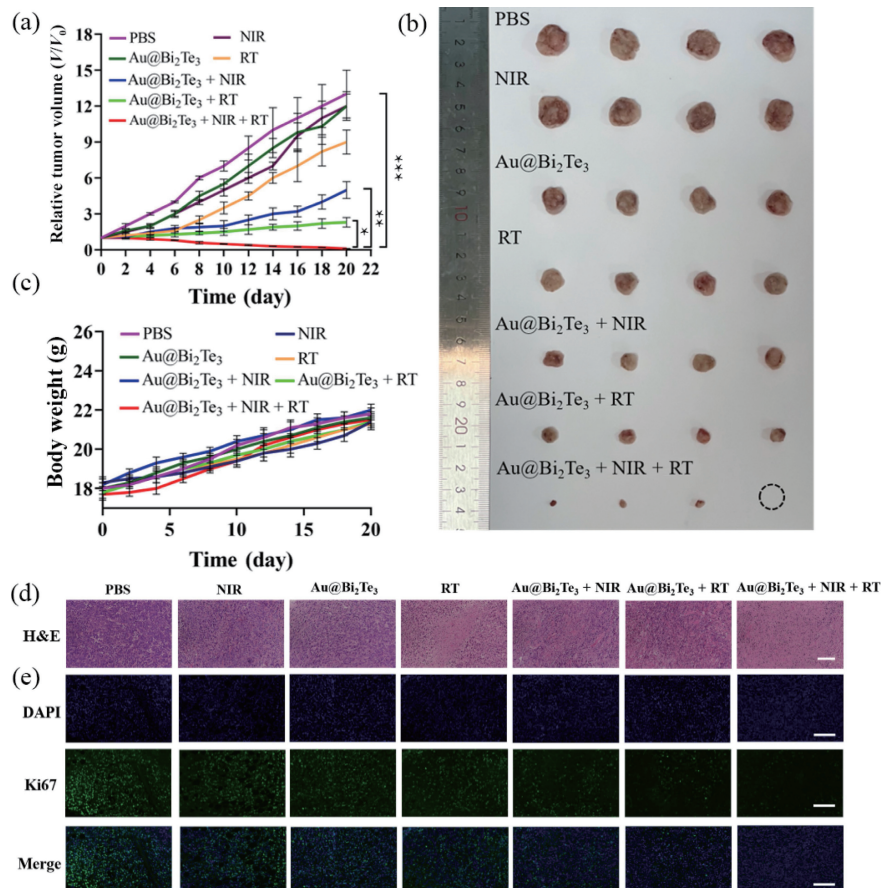


Figure 4 *In vivo* primary tumor therapeutic effect of Au@Bi₂Te₃ NPs. (a) Tumor growth curves of mice post-treatment during 20 days ($n = 5$). (b) Digital graphs of tumor tissues in different groups 20 days post-treatments. (c) Average body weight from different groups 20 days post-treatments. (d) and (e) H&E and Ki67 staining of tumors post-treatment. Scale bar (H&E): 200 μ m, scale bar (Ki67): 100 μ m, * $P < 0.05$, ** $P < 0.01$, *** $P < 0.001$.

5(c), and Figs. S16(b) and S16(c) in the ESM). Increased percentages of CD80 and CD86 were found in the groups with RT treatment (RT, Au@Bi₂Te₃-PEG + RT, and Au@Bi₂Te₃-PEG + NIR + RT). The percentage of CD80 and CD86 in the RT and Au@Bi₂Te₃-PEG + RT group was 2.50-fold and 5.72-fold of that of the PBS group, respectively. Of note, although mild-PTT could hardly induce DC maturation directly, the combination of Au@Bi₂Te₃ + NIR + RT could significantly increase the percentage of CD80 and CD86 to 6.24-fold compared with the PBS group (Figs. 5(b) and 5(c)). These results indicated that synergistic treatment was a promising avenue by which the immune process could be modulated. Conversely, the groups Au@Bi₂Te₃-PEG and Au@Bi₂Te₃-PEG + NIR did not show any obvious effect on the

DCs, thereby indicating that NPs or mild-PTT did not induce DC maturation directly.

Furthermore, previous studies have demonstrated that the increased expression of HIF-1α in hypoxic TME could lead to significantly upregulated PD-L1 on tumor cells [13, 27, 38]. Then, PD-L1 upregulation leads to decreased T cells, thus, boosting immunotherapeutic resistance of tumors. Downregulation of PD-L1 has been reported as an efficient way to increase T lymphocyte infiltration, thus alleviating immunotherapeutic resistance of tumors [12, 39, 40]. Because Au@Bi₂Te₃-PEG can alleviate tumor hypoxia and downregulate HIF-1α, PD-L1 expression is expected to be suppressed consequently. Immunofluorescence assay and western blotting results demonstrated that significant

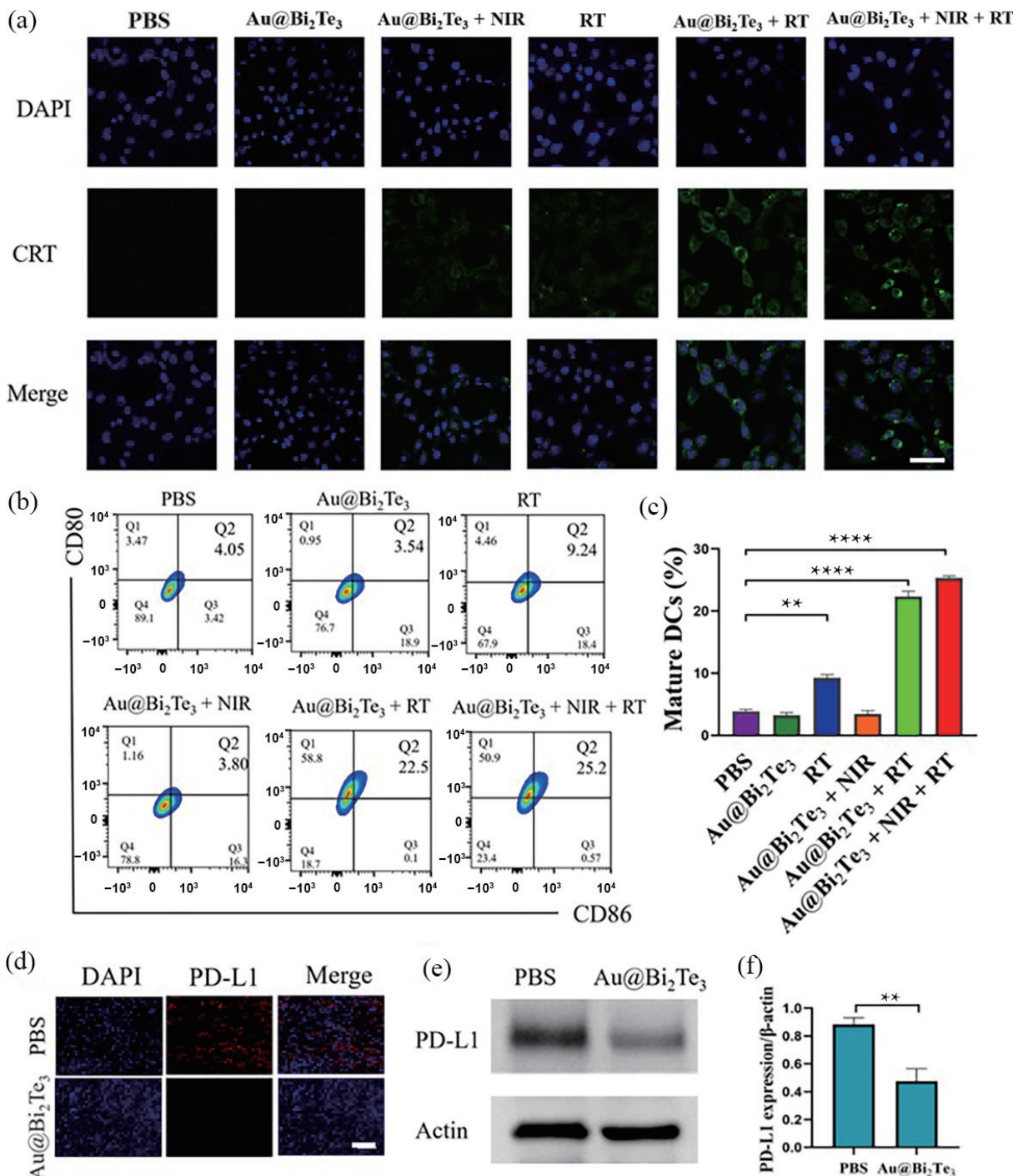


Figure 5 ICD induced by synergistic mild-PTT/RT effect of Au@Bi₂Te₃ *in vitro*. (a) CRT fluorescent images of 4T1 cells with different treatments. (b) and (c) Flow cytometry data indicates DC maturation (CD80⁺ CD86⁺) of 4T1 cells with different treatments. (d) Immunofluorescent analysis of PD-L1 expression in tumors. (e) and (f) Western blot analysis of PD-L1 protein in 4T1 tumors. Scale bar: 100 μm, **P < 0.01, ****P < 0.0001.

downregulation of PD-L1 was observed in the Au@Bi₂Te₃-PEG group (Figs. 5(d)–5(f)). Consequently, enhanced tumor hypoxia could obviously increase T lymphocyte infiltration, which combined with RT-induced ICD could inhibit tumor immune escape and enhance antitumor response.

3.6 In vivo distant tumor combination therapy

Tumor metastasis affects long-term survival in cancer. According to our results above, the combination of Au@Bi₂Te₃ + NIR + RT could efficiently induce ICD and activate autoimmunity, which has the potential to treat distal tumors. A bilateral 4T1 tumor model was established (right: primary tumors; left: distant tumors).

In mice receiving Au@Bi₂Te₃-PEG + RT treatment, the distant tumors decreased to some extent. Moreover, the Au@Bi₂Te₃-PEG + NIR + RT treatment could significantly inhibit the growth of distant tumors, which is in consistent with DC activation results, indicating the vital role of RT and mild-PTT enhanced immunotherapy (Figs. 6(a)–6(c), and Fig. S17 in the ESM). No obvious body weights loss was observed in the treatment groups. In brief, the Au@Bi₂Te₃-PEG NPs with mild-PTT/RT could promote ICD response for improved tumor immunogenicity and DC maturation. Combined with downregulation of immune-blocking inhibitors, such as PD-L1, the antitumor immune response could be activated to inhibit the growth of the distant tumors. Furthermore, immunofluorescence assay and flow cytometry showed that obviously increased CD8⁺ and CD4⁺ T cell infiltration was found in distant tumor tissues of the Au@Bi₂Te₃-PEG + NIR + RT group (Figs. 7(a)–7(e)). In addition, IFN- γ , TNF- α , and IL-6 were measured by ELISA. It was shown that among all the groups, in the Au@Bi₂Te₃-PEG + NIR + RT group, the highest level of IFN- γ , TNF- α and IL-6 secretion were induced in the serum (Fig. 7(f) and Fig. S18 in the ESM), indicative of a robust antitumor immunity. These results strongly suggested the synergistic effect of Au@Bi₂Te₃-PEG NPs and mild-PTT/RT in

triggering efficient ICD and systemic antitumor immunity to suppress both primary and distant tumors.

4 Conclusions

In this study, Au@Bi₂Te₃-PEG nanozymes were developed as a theranostic nanoplateform for spectral CT/PA molecular imaging and for photothermal/radio/immunotherapy simultaneously. The synergistic effect between Au@Bi₂Te₃-PEG and RT could induce tumor ICD to some extent, while further combination of mild-PTT could efficiently induce ICD. Moreover, Au@Bi₂Te₃-PEG-induced tumor hypoxia relief could not only increase the effect of RT by enhanced ROS generation, but also reduce hypoxia-related cytokines and downregulate the expression of immunosuppressive PD-L1 to unleash immune-promoting T cells. By combining enhanced ICD induction and downregulation of PD-L1, a systemic tumor-specific T-cell response could be activated with infiltration of CD8⁺ T cells and CD4⁺ T cells into distant tumors, that efficiently suppressed the growth of both primary and distant tumors. Therefore, combination therapy of nanoregulator-based mild-PTT/RT might provide a new strategy for improved cancer immunotherapy.

Acknowledgements

This work was supported by the National Natural Science Foundation of China (Nos. 81871334, 81801764, 82072056, and 51937010), the Guangdong Basic and Applied Basic Research Foundation (Nos. 2017A050506011, 2018030310343, 2020B1515020008, 2021A1515012542, and 2021A1515011882), the Medical Scientific Research Foundation of Guangdong Province (No. A2018014), and the Pearl River Talented Young Scholar Program (No. 2017GC010282).

Electronic Supplementary Material: Supplementary material (HRTEM image of Au@Bi₂Te₃ NPs, fluorescence images of [Ru(dpp)₃]Cl₂ in 4T1 cells, HMGB1 fluorescent images of 4T1

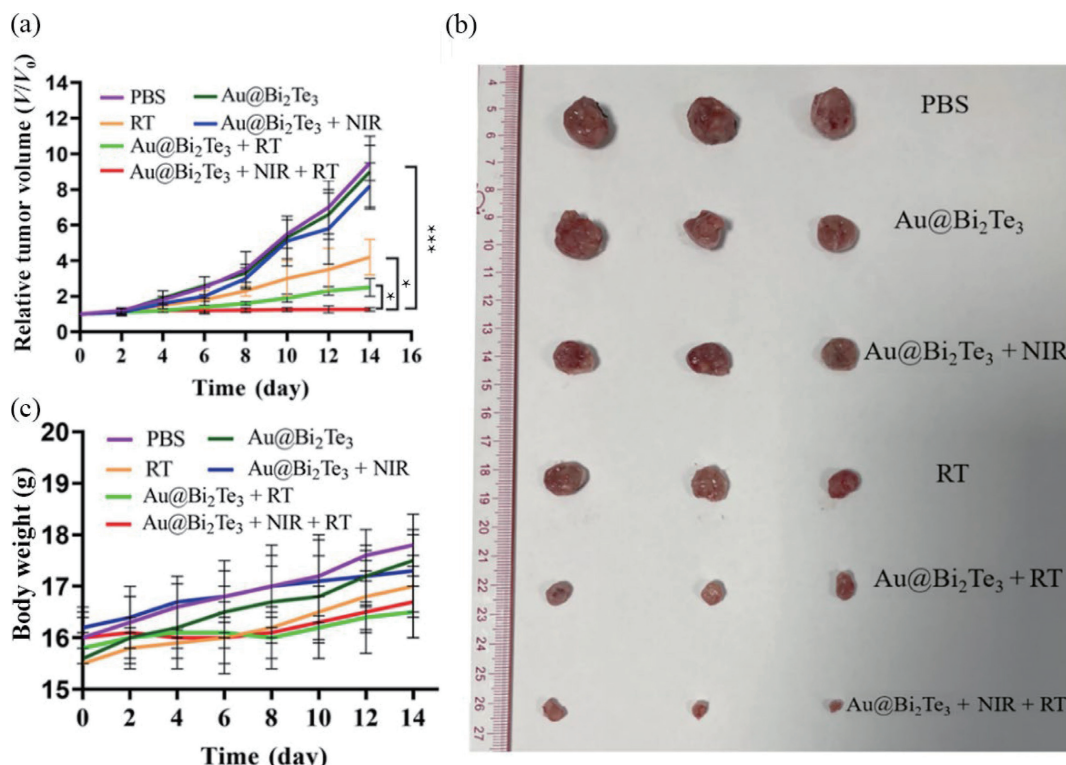


Figure 6 Combination therapy-mediated antitumor effect in distant 4T1 tumor model. (a) Tumor growth curves of mice post-treatment during 20 days ($n = 3$). (b) Digital graphs of tumor tissues in different groups 20 days post-treatments. (c) Body weight of mice from different groups 20 days post-treatments. * $P < 0.05$, ** $P < 0.001$.

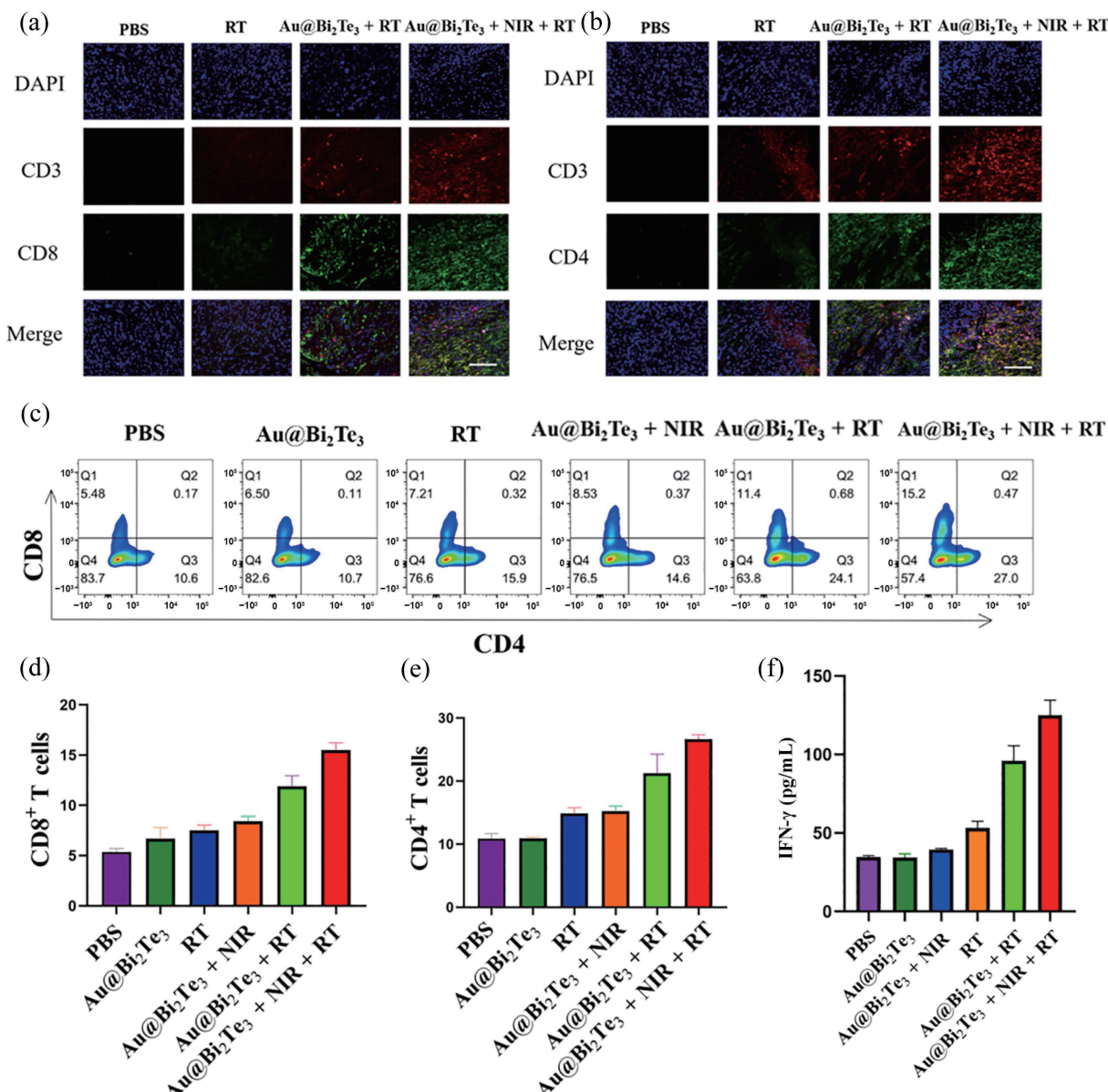


Figure 7 (a) Immunofluorescent staining images of CD8⁺ T cells *in vivo* tumors. (b) Immunofluorescent staining images of CD4⁺ T cells *in vivo* tumors. (c)–(e) Flow cytometry data indicates CD4 and CD8 in distant tumors with different treatments. (f) The INF-γ levels in the serum. Scale bar = 100 μm.

cells, CRT fluorescent images of tumors *in vivo*, the TNF-α and IL-6 levels, biodistribution of 4T1 tumor-bearing mice injected with Au@Bi₂Te₃-PEG, and original pictures of western blot) is available in the online version of this article at <https://doi.org/10.1007/s12274-022-4645-3>.

References

- [1] Sharma, P.; Hu-Lieskovan, S.; Wargo, J. A.; Ribas, A. Primary, adaptive, and acquired resistance to cancer immunotherapy. *Cell*. **2017**, *168*, 707–723.
- [2] Zhu, L. P.; Liu, J.; Zhou, G. Y.; Liu, T. M.; Dai, Y. L.; Nie, G. J.; Zhao, Q. Remodeling of tumor microenvironment by tumor-targeting nanozymes enhances immune activation of CAR T cells for combination therapy. *Small*. **2021**, *17*, 2102624.
- [3] Song, C.; Phuengkham, H.; Kim, Y. S.; Dinh, V. V.; Lee, I.; Shin, I. W.; Shin, H. S.; Jin, S. M.; Um, S. H.; Lee, H. et al. Syringeable immunotherapeutic nanogel reshapes tumor microenvironment and prevents tumor metastasis and recurrence. *Nat. Commun.* **2019**, *10*, 3745.
- [4] Guevara, M. L.; Persano, F.; Persano, S. Nano-immunotherapy: Overcoming tumour immune evasion. *Semin. Cancer Biol.* **2021**, *69*, 238–248.
- [5] Baxevanis, C. N.; Fortis, S. P.; Perez, S. A. The balance between breast cancer and the immune system: Challenges for prognosis and clinical benefit from immunotherapies. *Semin. Cancer Biol.* **2021**, *72*, 76–89.
- [6] Wan, C. X.; Keany, M. P.; Dong, H.; Al-Alem, L. F.; Pandya, U. M.; Lazo, S.; Boehnke, K.; Lynch, K. N.; Xu, R.; Zarrella, D. T. et al. Enhanced efficacy of simultaneous PD-1 and PD-L1 immune checkpoint blockade in high-grade serous ovarian cancer. *Cancer Res.* **2021**, *81*, 158–173.
- [7] Vranic, S.; Cyprian, F. S.; Gatalica, Z.; Palazzo, J. PD-L1 status in breast cancer: Current view and perspectives. *Semin. Cancer Biol.* **2021**, *72*, 146–154.
- [8] Mpekris, F.; Panagi, M.; Voutouri, C.; Martin, J. D.; Samuel, R.; Takahashi, S.; Gotohda, N.; Suzuki, T.; Papageorgis, P.; Demetriou, P. et al. Normalizing the microenvironment overcomes vessel compression and resistance to nano-immunotherapy in breast cancer lung metastasis. *Adv. Sci.* **2021**, *8*, 2001917.
- [9] Salas-Benito, D.; Pérez-Gracia, J. L.; Ponz-Sarvisé, M.; Rodriguez-Ruiz, M. E.; Martínez-Forero, I.; Castañón, E.; López-Picazo, J. M.; Sanmamed, M. F.; Melero, I. Paradigms on immunotherapy combinations with chemotherapy. *Cancer Discov.* **2021**, *11*, 1353–1367.
- [10] Tang, T. Y.; Huang, X.; Zhang, G.; Hong, Z. T.; Bai, X. L.; Liang,

- T. B. Advantages of targeting the tumor immune microenvironment over blocking immune checkpoint in cancer immunotherapy. *Sig. Transduct. Target. Ther.* **2021**, *6*, 72.
- [11] Cousin, N.; Cap, S.; Dihl, M.; Tacconi, C.; Detmar, M.; Dieterich, L. C. Lymphatic PD-L1 expression restricts tumor-specific CD8⁺ T-cell responses. *Cancer Res.* **2021**, *81*, 4133–4144.
- [12] Norman, M. Z.; Desantis, G.; Janji, B.; Hasmim, M.; Karray, S.; Dessen, P.; Bronte, V.; Chouaib, S. PD-L1 is a novel direct target of HIF-1 α , and its blockade under hypoxia enhanced MDSC-mediated T cell activation. *J. Exp. Med.* **2014**, *211*, 781–790.
- [13] Yu, M.; Duan, X. H.; Cai, Y. J.; Zhang, F.; Jiang, S. Q.; Han, S. S.; Shen, J.; Shuai, X. T. Multifunctional nanoregulator reshapes immune microenvironment and enhances immune memory for tumor immunotherapy. *Adv. Sci.* **2019**, *6*, 1900037.
- [14] Qi, J.; Jin, F. Y.; Xu, X. L.; Du, Y. Z. Combination cancer immunotherapy of nanoparticle-based immunogenic cell death inducers and immune checkpoint inhibitors. *Int. J. Nanomed.* **2021**, *16*, 1435–1456.
- [15] Zheng, P.; Ding, B. B.; Jiang, Z. Y.; Xu, W. G.; Li, G.; Ding, J. X.; Chen, X. S. Ultrasound-augmented mitochondrial calcium ion overload by calcium nanomodulator to induce immunogenic cell death. *Nano Lett.* **2021**, *21*, 2088–2093.
- [16] Tang, H. L.; Xu, X. J.; Chen, Y. X.; Xin, H. H.; Wan, T.; Li, B. W.; Pan, H. M.; Li, D.; Ping, Y. Reprogramming the tumor microenvironment through second-near-infrared-window photothermal genome editing of PD-L1 mediated by supramolecular gold nanorods for enhanced cancer immunotherapy. *Adv. Mater.* **2021**, *33*, 2006003.
- [17] Obeid, M.; Tesniere, A.; Ghiringhelli, F.; Fimia, G. M.; Apetoh, L.; Perfettini, J. L.; Castedo, M.; Mignot, G.; Panaretakis, T.; Casares, N. et al. Calreticulin exposure dictates the immunogenicity of cancer cell death. *Nat. Med.* **2007**, *13*, 54–61.
- [18] Zhou, F. Y.; Feng, B.; Yu, H. J.; Wang, D. G.; Wang, T. T.; Ma, Y. T.; Wang, S. L.; Li, Y. P. Tumor microenvironment-activatable prodrug vesicles for nanoenabled cancer chemoimmunotherapy combining immunogenic cell death induction and CD47 blockade. *Adv. Mater.* **2019**, *31*, 1805888.
- [19] Choi, B.; Choi, H.; Yu, B.; Kim, D. H. Synergistic local combination of radiation and anti-programmed death ligand 1 immunotherapy using radiation-responsive splintery metallic nanocarriers. *ACS Nano* **2020**, *14*, 13115–13126.
- [20] Donlon, N. E.; Power, R.; Hayes, C.; Reynolds, J. V.; Lysaght, J. Radiotherapy, immunotherapy, and the tumour microenvironment: Turning an immunosuppressive milieu into a therapeutic opportunity. *Cancer Lett.* **2021**, *502*, 84–96.
- [21] Zhang, C. Y.; Yan, L.; Gu, Z. J.; Zhao, Y. L. Strategies based on metal-based nanoparticles for hypoxic-tumor radiotherapy. *Chem. Sci.* **2019**, *1*, 6932–6943.
- [22] Zhang, Q. H.; Chen, J. W.; Ma, M.; Wang, H.; Chen, H. R. A bioenvironment-responsive versatile nanoplatform enabling rapid clearance and effective tumor homing for oxygen-enhanced radiotherapy. *Chem. Mater.* **2018**, *30*, 5412–5421.
- [23] Liu, H. M.; Cheng, R.; Dong, X. H.; Zhu, S.; Zhou, R. Y.; Yan, L.; Zhang, C. Y.; Wang, Q.; Gu, Z. J.; Zhao, Y. L. BiO_{2-x} nanosheets as radiosensitizers with catalase-like activity for hypoxia alleviation and enhancement of the radiotherapy of tumors. *Inorg. Chem.* **2020**, *59*, 3482–3493.
- [24] Liang, Y.; Peng, C.; Su, N.; Li, Q. Y.; Chen, S. W.; Wu, D.; Wu, B.; Gao, Y.; Xu, Z. T.; Dan, Q. et al. Tumor microenvironments self-activated cascade catalytic nanoscale metal organic frameworks as ferroptosis inducer for radiosensitization. *Chem. Eng. J.* **2022**, *437*, 135309.
- [25] Hu, H. L.; Zheng, S. T.; Hou, M. R.; Zhu, K.; Chen, C. Y.; Wu, Z. D.; Qi, L.; Ren, Y. Y.; Wu, B.; Xu, Y. K. et al. Functionalized Au@Cu-Sb-S nanoparticles for spectral CT/photoacoustic imaging guided synergetic photo-radiotherapy in breast cancer. *Int. J. Nanomed.* **2022**, *17*, 395–407.
- [26] Pei, P.; Shen, W. H.; Zhang, Y.; Zhang, Y. X.; Qi, Z. Y.; Zhou, H. L.; Liu, T.; Sun, L.; Yang, K. Radioactive nano-oxygen generator enhance anti-tumor radio-immunotherapy by regulating tumor microenvironment and reducing proliferation. *Biomaterials* **2022**, *280*, 121326.
- [27] Meng, L. T.; Cheng, Y. L.; Tong, X. N.; Gan, S. J.; Ding, Y. W.; Zhang, Y.; Wang, C.; Xu, L.; Zhu, Y. S.; Wu, J. H. et al. Tumor oxygenation and hypoxia inducible factor-1 functional inhibition via a reactive oxygen species responsive nanoplatform for enhancing radiation therapy and abscopal effects. *ACS Nano* **2018**, *12*, 8308–8322.
- [28] Gong, N. Q.; Sheppard, N. C.; Billingsley, M. M.; June, C. H.; Mitchell, M. J. Nanomaterials for T-cell cancer immunotherapy. *Nat. Nanotechnol.* **2021**, *16*, 25–36.
- [29] Wang, J. P.; Sun, J. Y.; Hu, W.; Wang, Y. H.; Chou, T.; Zhang, B. L.; Zhang, Q.; Ren, L.; Wang, H. J. A porous Au@Rh bimetallic core-shell nanostructure as an H₂O₂-driven oxygenator to alleviate tumor hypoxia for simultaneous bimodal imaging and enhanced photodynamic therapy. *Adv. Mater.* **2020**, *32*, 2001862.
- [30] Dan, Q.; Hu, D. H.; Ge, Y. S.; Zhang, S. Y.; Li, S. Q.; Gao, D. Y.; Luo, W. X.; Ma, T.; Liu, X.; Zheng, H. R. et al. Ultrasmall theranostic nanozymes to modulate tumor hypoxia for augmenting photodynamic therapy and radiotherapy. *Biomater. Sci.* **2020**, *8*, 973–987.
- [31] Lin, Y. H.; Ren, J. S.; Qu, X. G. Nano-gold as artificial enzymes: Hidden talents. *Adv. Mater.* **2014**, *26*, 4200–4217.
- [32] Long, Y. J.; Li, Y. F.; Liu, Y.; Zheng, J. J.; Tang, J.; Huang, C. Z. Visual observation of the mercury-stimulated peroxidase mimetic activity of gold nanoparticles. *Chem. Commun.* **2011**, *47*, 11939–11941.
- [33] Lien, C. W.; Huang, C. C.; Chang, H. T. Peroxidase-mimic bismuth-gold nanoparticles for determining the activity of thrombin and drug screening. *Chem. Commun.* **2012**, *48*, 7952–7954.
- [34] Bai, J.; Jia, X. D.; Ruan, Y. D.; Wang, C.; Jiang, X. E. Photosensitizer-conjugated Bi₂Te₃ nanosheets as theranostic agent for synergistic photothermal and photodynamic therapy. *Inorg. Chem.* **2018**, *57*, 10180–10188.
- [35] Hou, M. R.; Yan, C. G.; Chen, Z. L.; Zhao, Q. L.; Yuan, M. M.; Xu, Y. K.; Zhao, B. X. Multifunctional NIR-responsive poly(vinylpyrrolidone)-Cu-Sb-S nanotheranostic agent for photoacoustic imaging and photothermal/photodynamic therapy. *Acta Biomater.* **2018**, *74*, 334–343.
- [36] Xia, J.; Yao, J. J.; Wang, L. H. V. Photoacoustic tomography: Principles and advances (invited review). *Prog. Electromagn. Res.* **2014**, *147*, 1–22.
- [37] Gargiulo, S.; Albanese, S.; Mancini, M. State-of-the-art preclinical photoacoustic imaging in oncology: Recent advances in cancer theranostics. *Contrast Media Mol. Imaging* **2019**, *2019*, 1–24.
- [38] Wang, B.; Zhao, Q.; Zhang, Y. Y.; Liu, Z. J.; Zheng, Z. Z.; Liu, S. Y.; Meng, L. B.; Xin, Y.; Jiang, X. Targeting hypoxia in the tumor microenvironment: A potential strategy to improve cancer immunotherapy. *J. Exp. Clin. Cancer Res.* **2021**, *40*, 24.
- [39] Liu, X.; Ye, N. B.; Liu, S.; Guan, J. K.; Deng, Q. Y.; Zhang, Z. J.; Xiao, C.; Ding, Z. Y.; Zhang, B. X.; Chen, X. P. et al. Hyperbaric oxygen boosts PD-1 antibody delivery and T cell infiltration for augmented immune responses against solid tumors. *Adv. Sci.* **2021**, *8*, 2100233.
- [40] Hu, C.; He, X. Q.; Chen, Y. X.; Yang, X. T.; Qin, L.; Lei, T.; Zhou, Y.; Gong, T.; Huang, Y.; Gao, H. L. Metformin mediated PD-L1 downregulation in combination with photodynamic-immunotherapy for treatment of breast cancer. *Adv. Funct. Mater.* **2021**, *31*, 2007149.